Journal of Zhejiang University SCIENCE
ISSN 1009-3095
http://www.zju.edu.cn/jzus
E-mail: jzus@zju.edu.cn

XMT enabled prediction of structure and permeability of flocculated structures and sediments

WILLIAMS R.A.[1], SELOMULYA C.[2], JIA X.[1]

([1]*Institute of Particle Science & Engineering, School of Process, Environmental & Materials Engineering, University of Leeds, Leeds LS2 9JT, UK*)

([2]*ARC Centre for Functional Nanomaterials, School of Chemical Engineering & Industrial Chemistry, University of New South Wales, Sydney NSW 2052, Australia*)

E-mail: R.A.Williams@leeds.ac.uk; c.selomulya@unsw.edu.au; X.Jia@leeds.ac.uk

Received Aug. 8, 2005; revision accepted Sept. 11, 2005

Abstract: 3D visualisations of the microstructure of flocculated particulates and sediments using optical confocal laser microscopy and high resolution X-ray microtomography (XMT) methods are described. Data obtained from in-situ measurements should enable direct computation of the properties of solids assembly (shape, size, contact area) and their permeability to fluids. A specific application relating to the formation of silica aggregates is described from which the behaviour of sediments containing these materials can be predicted on the basis of a bench-top test and the use of a Lattice Boltzman simulation. It is proposed that the method can potentially be used to predict trends such as the filtration behaviour of porous structures under different states of compression. This offers a significant benefit in assisting the formulation design of flocculated materials pertinent to a number of industrial sectors wishing to design optimal filtration or relevant operations.

Key words: Fluid flow, Imaging, Microstructure, Porous media, Visualization, Tomography
doi:10.1631/jzus.2005.A1367 **Document code:** A **CLC number:** TB126

INTRODUCTION

Separation of solids from suspending liquid plays a crucial role in a variety of processes, from nanomaterials synthesis to bio-processing. It often involves colloidal particles that need to be aggregated into more manageable sizes. Characteristics of these aggregates influence downstream solids recovery. For instance, aggregates with open configurations may settle slower than those with denser structures due to increasing fluid drag, although considerable flow-through could accelerate sedimentation rates for highly porous, large aggregates (Bushell *et al*., 2002). Compaction due to restructuring is significant when aggregates are subjected to low shear rates (Selomulya *et al*., 2002). Low-density aggregates may also produce easily compressible networks, forming less permeable deposits when exposed to dewatering or cake filtration (Gregory, 1998).

Most existing data on filtration, sedimentation, and thickening are focused on the macroscopic phenomena, whereas challenges still remain for fundamental understanding at a much smaller length scale. Insight into the micro-properties of aggregate and sediment is important for understanding system behaviour. Correlating physical properties to the hydrodynamic behaviour of aggregates poses a significant challenge due to their non-spherical and porous structures. Currently, attributes such as porosity or permeability are usually quantified by indirect means.

This paper demonstrates the feasibility of directly predicting the above properties using a combination of the latest commercially available imaging and numerical simulation techniques, namely, confocal scanning laser microscopy (CSLM), X-ray microtomography (XMT) and Lattice Boltzmann Method (LBM). Examples are given to illustrate the use of CSLM and XMT imaged structures with LBM

to visualise fluid flow or pressure distribution across complex solid structures. Potentially, it could assist in the understanding of settling behaviour for permeable aggregates, as well as sediment consolidation.

HYDRODYNAMIC IMAGING OF HYDRATED SPECIMENS

Confocal scanning laser microscopy

Polydisperse silica particles (d[4,3]=(22±11) μm measured by Malvern^{TM} 2000) of 0.5 g/L and 10 g/L initial concentrations were flocculated according to standard jar test procedure with iron chloride/Magnafloc 155 and Zetag 7654, respectively, giving average floc sizes of (276±137) μm and (72±35) μm. Samples were prepared for analysis in a high speed confocal scanning laser microscopy unit (Leica TCS SP2). Aggregates were carefully transferred using wide-mouth pipettes to a custom-made slide, comprising a brass plate with 8 mm diameter wells of 1.6 mm depth fused on a glass slide. This arrangement kept the aqueous samples from being compressed by the cover slip, whilst ensuring that they remained relatively inert during each scanning period (<5 min).

A fluorescent dye (Rhodamine B) was added to aggregates from 0.5 g/L flocculated suspension (with the filter set at 514 nm), and observation was done using a 20× oil immersion lens with a numerical aperture of 0.7. Staining was not performed on the 10 g/L solids content sample, as preliminary tests showed that the dye did not distribute evenly throughout this more concentrated assembly. The confocal microscopy system was set at a reflection mode with equal magnification for this sample. The optical sections for both specimens are shown in Fig.1. The corresponding 3D segments are given in Fig.2.

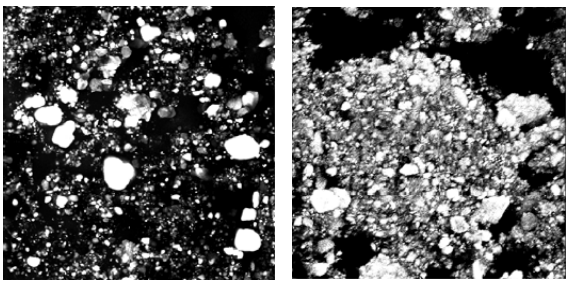

(a) (b)

Fig.1 Optical sections of settled silica aggregates at (a) 0.5 g/L (610 μm×610 μm) and (b) 10 g/L (480 μm×480 μm)

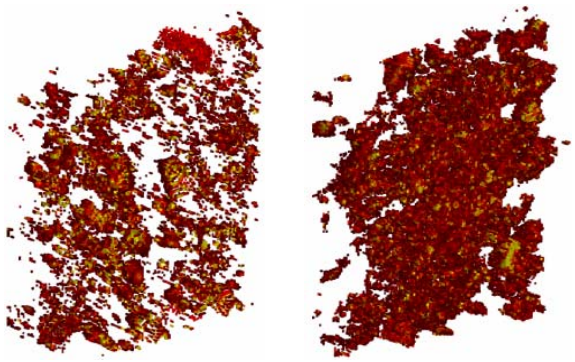

(a) (b)

Fig.2 Reconstructed 3D CSLM images at 45° view of settled silica aggregates at (a) 0.5 g/L and (b) 10 g/L

The voxel size was set at 1.0~1.6 μm while signals at z-direction were collected up to the distance of 50 μm. The scanning region and depth for confocal imaging are considerably limited by several factors. Higher magnification requires the optics to move closer to the specimen, thus reducing the scanning area. Confocal imaging suffers deterioration in signal-to-background ratio as it probes deeper into a sample, partly because the intensity of incoming laser from excitation source deteriorates as it is absorbed by fluorophores located other than at the plane of focus. Background interference also increases due to light scattering originated from regions away from the point being instantaneously illuminated. Accordingly, only a section of around 50 μm thickness can be observed in this case (Fig.2)—the scanning depth is currently limited to a few hundred microns for more sparsely distributed specimen.

For sediments or compact aggregates, the limitations are exacerbated by multiple scattering and obscuration of individual components within the packed sample. Yet the technique might be useful for quantitative image analysis due to its capability of resolving individual sub-micron particles. Current applications include the calculation of bacterial cell numbers, microbial areal fractions, and cell volumes from fluorescence signals with nucleic acid staining (‘tagging’). Potentially, it can be used to determine the mass fractal dimension from the spatial position of each particle for small discrete aggregates in chemically heterogeneous or opaque systems (for which light scattering techniques are somewhat inappropriate), assuming that the estimation from a thin slice is applicable for an entire object (Thill *et al*., 1998).

High resolution X-ray microtomography

We report below the data obtained using a desktop XMT system, SkyScan® 1072. Here, a spatial resolution less than 5 μm is attainable, similar to that of a synchrotron XMT. However, the size of scanned object decreases to less than 4 mm across at the highest magnifications. As data acquisition normally takes around 30 min or more, any vibration or disturbance to the sample has to be avoided during this period, to prevent the presence of artifacts in the reconstructed image. This also means that any dynamic changes to the structure of sample in this timescale should be avoided, although there are examples of non-equilibrium studies being undertaken (Leonard *et al*., 2003). XMT is capable of probing the internal structure of much larger objects than CSLM with greater depth penetration, provided there are sufficient contrasts in the shadow images for tomographical reconstruction. The contrast between an object and background depends on distinction in the attenuation values between the two, normalized by the background attenuation. It is a function of the photon energy of X-ray beam, as well as electron density and effective atomic number of the material, hence resolving a solid specimen in dry condition would be easier than in saturated or liquid phase, for example. In the range of X-ray energies generated by SkyScan® 1072 (<100 keV), the difference in atomic numbers is important as interactions between X-rays and materials mostly occur via photoelectric absorption. Enhanced contrasts may be achieved by adding an element with high atomic number to the water phase or using a dual-energy imaging approach (Wildenschild *et al*., 2002).

Silica aggregates were carefully transferred to a 0.25 ml thin-walled glass vial with 5 mm inner diameter, after which they were left to settle for at least 48 h before XMT analysis. This arrangement was needed to ensure minimal movement effects during 180° rotation of the object (with 0.45° step size) during image capture. The voxel size was 5.5 μm at 48× magnification and 5.7 μm at 45× magnification for 10 g/L and 0.5 g/L specimens, respectively. Cone-beam (Feldkamp) reconstruction algorithm was used at an intensity threshold (based on cross-section to image) excluding background measured as water in the glass insert.

3D rendered XMT images of sediments from suspensions with an initial silica solids concentration of 0.5 g/L (1.2 mm×1.2 mm×4.4 mm) and 10 g/L (1.2 mm×1.2 mm×3.5 mm) are shown in Fig.3. Conventionally, a sediment porosity profile is constructed through thickness estimated for each sediment layers by optical or other means, assuming a certain packing density model. Analysis of each 2D slice from XMT showed a decreasing porosity with depth, a trend that agrees with experimental observations (Hermawan *et al*., 2004), considering that structural collapse or compaction of sediment network is most likely to occur at lower depth. The overall average porosities were estimated to be 92.4% and 77.2% for low and high silica loadings, respectively.

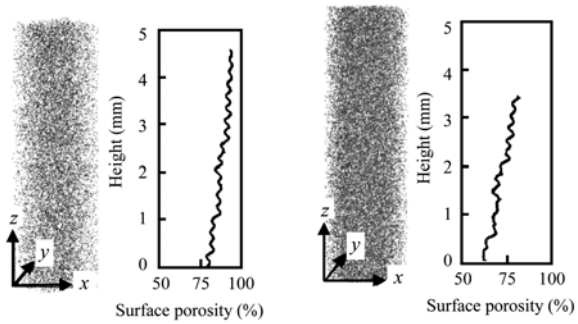

Fig.3 Reconstructed 3D XMT images and porosity profiles of settled silica aggregates at (a) 0.5 g/L and (b) 10 g/L loadings

Due to the small sample size, the use of a high-resolution XMT is currently limited to research purposes, where the interests rest in looking at microscopic properties. Considerable postprocessing is still required to image detailed structure and interconnectivity within millimetre-scale configurations, with specially developed algorithm required to reproduce the network in 3D from 2D data (Lin and Miller, 2004). In the near future, X-ray microtomography could potentially be used to track dynamic changes or fluid transport inside porous media, utilizing multiple radiation sources and sensors that simultaneously collect data and speed up the scanning time (Williams and Jia, 2003).

FLOW SIMULATION THROUGH POROUS STRUCTURES

One possible use of these images is to identify

and visualize preferable fluid pathways in an irregular structure through direct simulations of various fluid flow phenomena, using the Lattice Boltzmann Method (LBM) (Qian *et al*., 1992). A commercial software package, PowerFLOW®, was used to model fluid flowing through 3D porous solid media. The basic premise is in tracking discrete virtual 'particles' (represented by a density distribution function) in discretised space to represent digitally fluid dynamics. Using a lattice approach, solid geometry, whether computer generated or directly imaged, can be directly imported as a closed surface defined by triangular facets, with each surface voxel generated independently of their neighbours. This circumvents the complexities of grid generation in traditional CFD programs. By setting appropriate boundary conditions, any form of real fluid dynamic process may, in principle, be replicated.

An example here used a digitized section from 3D image captured by XMT as the solid geometry (Fig.4). When importing an image file, the dimensionless size can be mapped to any units of measure, including lattice-units to indicate the characteristic length of resolution (Lin and Miller, 2004). The important consideration is to ensure a correct relationship between sizes among the regions in a simulation case. For simplicity, the solid structure here of size 30×30×30 (unit) was scaled in millimetre. The purpose was to show the simulation's capability to model fluid behaviour in a physical sense and to observe whether they generate trends as expected in practice, rather than to validate the exact values of parameters.

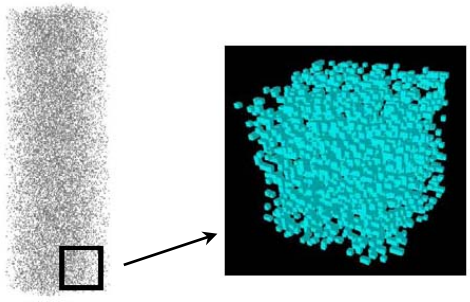

Fig.4 A digitized segment from 3D XMT image of 0.5 g/L specimen

The simulation volume enclosing the solid geometry was set at 1000×1000×1000 (unit), with frictionless wall boundary (free-slip wall) to minimize the impact of walls on fluid flow. The solid geometry was placed at the centre of the simulation volume. Flow was set in the simulation volume along z-direction by specifying an inlet (where fluid is 'injected' into simulation) and an outlet (to 'receive' fluid from simulation), acting as driving boundaries on the opposite sides of the wall. The other 4 sides were specified as frictionless wall boundaries with zero mass and energy flux. The velocity and pressure distributions were generated by setting fluid to flow at inlet velocities of 0.01 m/s, 0.05 m/s, and 0.10 m/s, respectively, and at an outlet static pressure of 101325 Pa (Table 1).

Table 1 Simulation conditions for fluid flow through digitized 3D structures

Simulation conditions	3D laminar flow, isothermal
Characteristic pressure	101325 Pa
Characteristic temperature	293 K
Characteristic density	1000 kg/m^3
Characteristic velocity	(a) 0.01 m/s; (b) 0.05 m/s; (c) 0.10 m/s
Characteristic viscosity	10^{-6} m^2/s
Specific heat	4183 J/(kg·K)
Reynolds number	(a) 300; (b) 1500; (c) 3000
Total time steps	10000
Equivalent of one time step	2.9×10^{-3} s for 0.01 m/s 4.8×10^{-3} s for 0.05 m/s 2.4×10^{-3} s for 0.10 m/s

The results for 0.5 g/L and 10 g/L specimens, respectively, when there were no significant changes in fluid properties (after 10000 time steps) are summarised in Table 2. Permeability values were estimated according to Darcy's law (Lin and Miller, 2004)

$$k = -\frac{U\mu}{\Delta P/\Delta z} \tag{1}$$

where k is the permeability, U is the average fluid velocity across the solid structure, μ is the dynamic viscosity, and $\Delta P/\Delta z$ is the pressure gradient along z-direction. The value for permeability (k) can be obtained from the slope of a plot between $-\mu U\Delta z$ and ΔP.

The average velocity value for fluid travelling through the 0.5 g/L specimen was higher than for flow

inside the 10 g/L segment for similar inlet velocity, indicating a less resistance to flow. PowerFlow® outputs in Fig.5 and Fig.6 reveal a range of velocity magnitudes measured at the limit of resolution within the configuration for inlet velocities 0.01 m/s and 0.10 m/s. Faster flows, as indicated by warmer colours in the plots, display the preferential pathways as fluid navigated through the channels between adjacent solids.

Fluid was shown to penetrate into the main section of 0.5 g/L, particularly at a higher inlet velocity (Fig.6), with the internal velocity decreasing further along the structure. The 10 g/L configuration was less permeable, with flows occurring mostly around the edges or on the outside, rather than across the solid. The 3D contour plots in Fig.5b show that only a small fraction of fluid could reach the average velocity of 1.4E-4 m/s inside solid geometry when the ambient fluid was flowing at 0.01 m/s. The proportion of internal flow was more substantial when the surrounding velocity was higher (Fig.6b), thus providing the necessary differential pressure for flow through the structure.

The comparatively higher resistance at 10 g/L loading is also reflected by the higher pressure drop across the structure for all inlet velocities (Table 2). Fig.7 shows the distribution of internal pressure, indicating the extent of fluid pressure likely to be imposed on the solid structure at a specific flow velocity. Elevated pressure distribution was experienced on the side of fluid entry as expected, and was more significant for the lower solid loading. This type of simulation, integrated with real structural data from imaging, could potentially be useful for predicting trends such as sediment permeability, compressibility, or cake resistance during a filtration process.

Another example of possible applications is given using a smaller structure formed by an assembly of 700 particles (primary particle diameter: 20 μm) through a simulated aggregation process (Jia *et al*., 2000), resulting in an aggregate of d_F 2.1 (Fig.8).

By applying a specific streamline velocity of 0.01 m/s (within the range of terminal settling velocity values estimated from Stokes' equation for fractal aggregates of similar size) in one direction; eddies, which occur when fluid encounters obstructions and subsequently alters direction, can be located (blue indicating counter-clockwise and red for clockwise rotations, respectively). Swirling motions and vorticity (physically defined as a measure of angular velocity if a continuum fluid can be represented by discrete 'packets') cause drag that could influence sedimentation rate. This type of simulation would enable the effects of fluid drag and permeability to be quantified for aggregates of any shapes and structures, as a step towards a more comprehensive model that could accurately relate the aggregate physical properties and their settling velocity (Bushell *et al*., 2002). Likewise, the relative motion between small eddies acting on a solid body produces hydrodynamic (pressure and tensile) stresses that could induce fragmentation. Accurate visualization should enable a better appreciation of these elements.

These simulations demonstrate the potential for predicting the properties of real structures by combining tomographic images with versatile modelling tools. Data including internal flow and pressure distribution and other transport properties, which are not easily accessible experimentally, could be attained with this approach. The next step will be to link the solid physical properties at micro-scale with the observed fluid dynamics, in order to develop a fundamental relationship from directly measurable parameters.

Table 2 Simulation results for fluid flow through digitized 3D structures

Parameters	Inlet velocity (m/s)	Average internal velocity (m/s)	x-velocity* (m/s)	y-velocity (m/s)	z-velocity (m/s)	Average internal pressure (Pa)	Estimated pressure drop (Pa)	Estimated permeability (m^2)
0.5 g/L segment	0.01	6.5×10^{-4}	-1.6×10^{-5}	4.3×10^{-6}	4.8×10^{-4}	101325	7.9×10^{-2}	
	0.05	5.1×10^{-3}	2.1×10^{-5}	3.1×10^{-5}	4.1×10^{-3}	101336	2	4.1×10^{-8}
	0.10	1.2×10^{-2}	8.4×10^{-5}	5.7×10^{-5}	9.8×10^{-3}	101368	8	
10 g/L segment	0.01	1.4×10^{-4}	4.1×10^{-6}	-9.6×10^{-7}	8.3×10^{-5}	101325	4.0×10^{-1}	
	0.05	1.3×10^{-3}	1.9×10^{-5}	2.8×10^{-7}	8.3×10^{-4}	101336	12	2.0×10^{-9}
	0.10	3.4×10^{-3}	3.3×10^{-5}	7.6×10^{-5}	2.2×10^{-3}	101368	48	

* Negative values indicating flow in opposite direction

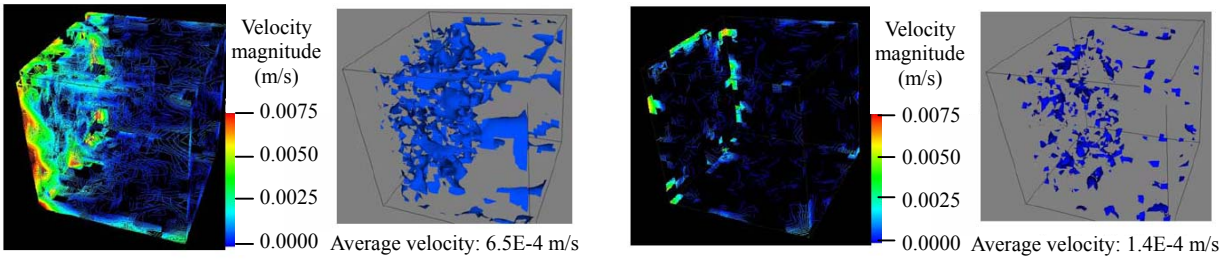

(a) (b)

Fig.5 PowerFlow® outputs showing velocity distribution and average velocity for (a) 0.5 g/L and (b) 10 g/L digitized segments. Simulation volume fluid velocity was 0.01 m/s

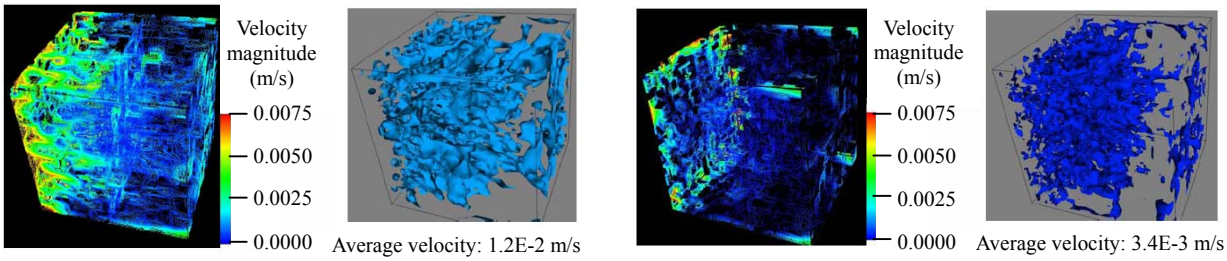

(a) (b)

Fig.6 PowerFlow® outputs showing velocity distribution and average velocity for (a) 0.5 g/L and (b) 10 g/L digitized segments. Simulation volume fluid velocity was 0.10 m/s

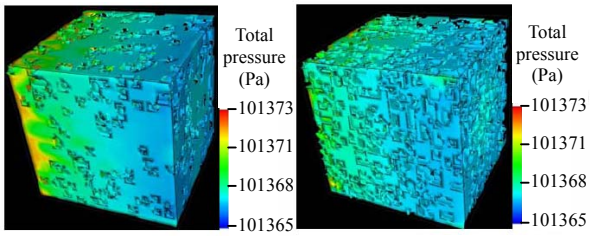

(a) (b)

Fig.7 PowerFlow® outputs showing pressure distribution for (a) 0.5 g/L and (b) 10 g/L digitized segments. Simulation volume fluid velocity was 0.10 m/s

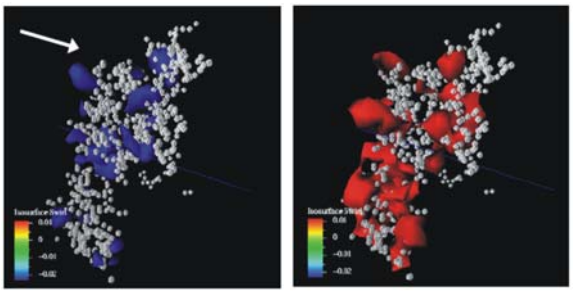

Fig.8 Powerflow® simulations showing swirling motions on a computer-generated aggregate with d_F of 2.1

CONCLUSION

Structural imaging of aggregated systems in their native state can be conducted using confocal scanning laser microscopy and X-ray microtomography to produce high-resolution 3D images in a relatively non-destructive manner. High-resolution X-ray microtomographic method in particular, combined with robust fluid simulation, is a promising tool to provide invaluable insights into aggregate and sediment microstructure. The ability to derive performance information, such as fluid permeability, from laboratory based measurements of microstructure coupled with appropriate micro-scale physical and chemical simulations offers considerable potentials. Future work will include employing algorithms to analyse pore size distribution and structure within the sediments. It is anticipated that such methods will become increasingly important in enabling direct analysis of flow through aggregates and for predicting sediment compaction.

ACKNOWLEDGEMENT

The provision of a Visiting Fellowship from the Royal Academy of Engineering for CS is gratefully acknowledged.

References

Bushell, G.C., Yan, Y.D., Woodfield, D., Raper, J., Amal, R., 2002. On techniques for the measurement of the mass fractal dimensions of aggregates. *Advances in Colloid and Interface Science*, **95**:1-50.

Gregory, J., 1998. The role of floc density in solid-liquid separation. *Filtration & Separation*, **35**(4):367-371.

Hermawan, M., Bushell, G., Bickert, G., Amal, R., 2004. Characterisation of short-range structure of silica aggregates – implication to sediment compaction. *International Journal of Mineral Processing*, **73**:65-81.

Jia, X., Wedlock, D.J., Williams, R.A., 2000. Simulation of simultaneous aggregation and sedimentation. *Minerals Engineering*, **13**:1349-1360.

Leonard, A., Blacher, S., Marchot, P., Pirard, J.P., Crine, M., 2003. Moisture Profile Determination During Convective Drying Using X-ray Microtomography. Proc. Third World Congress in Industrial Process Tomography, p.730-735.

Lin, C.L., Miller, J.D., 2004. Pore structure analysis of particle beds for fluid transport simulation during filtration. *International Journal of Mineral Processing*, **73**(2-4): 281-294.

Qian, Y., D'Humieres, D., Lallemand, P., 1992. Lattice-BGK models for Navier-Stokes equations. *Europhysics Letter*, **17**(6):479-484.

Selomulya, C., Bushell, G., Amal, R., Waite, T.D., 2002. Aggregation mechanisms of latex of different particle sizes in a controlled shear environment. *Langmuir*, **18**(6):1974-1984.

Thill, A., Veerapaneni, S., Simon, B., Wiesner, M., Bottero, J.Y., Snidaro, D., 1998. Determination of structure of aggregates by confocal scanning laser microscopy. *Journal of Colloid and Interface Science*, **204**:357-362.

Wildenschild, D., Hopmans, J.W., Vaz, C.M.P., Rivers, M.L., Rikard, D., Christensen, B.S.B., 2002. Using X-ray computed tomography in hydrology: systems, resolutions, and limitations. *Journal of Hydrology*, **267**:285-297.

Williams, R.A., Jia, X., 2003. Tomographic imaging of particulate systems. *Advanced Powder Technology*, **14**(1): 1-16.